Forward problem solution for electrical conductivity imaging via contactless measurements

Nevzat G Gençer† and M Nejat Tek

Department of Electrical and Electronics Engineering, Middle East Technical University, 06531, Ankara, Turkey

Abstract.   The forward problem of a new medical imaging system is analysed in this study. This system uses magnetic excitation to induce currents inside a conductive body and measures the magnetic fields of the induced currents. The forward problem, that is determining induced currents in the conductive body and their magnetic fields, is formulated. For a general solution of the forward problem, the finite element method (FEM) is employed to evaluate the scalar potential distribution. Thus, inhomogeneity and anisotropy of conductivity is taken into account for the FEM solutions. An analytical solution for the scalar potential is derived for homogeneous conductive spherical objects in order to test FEM solutions. It is observed that the peak error in FEM solutions is less than 2%. The numerical system is used to reveal the characteristics of the measurement system via simulations. Currents are induced in a $9 \times 9 \times 5$ cm body of conductivity 0.2 S m^{-1} by circular coils driven sinusoidally. It is found that a 1 cm shift in the perturbation depth reduces the field magnitudes to approximately one-tenth. In addition, the distance between extrema increases. Further simulations carried out using different coil configurations revealed the performance of the method and provided a design perspective for a possible data acquisition system.

1. Introduction

Imaging electrical conductivity of tissues has been a popular research area in the last decade. Different methodologies have been proposed to image the spatio-temporal evolution of conductivity changes in the human body (Morucci and Rigaud 1996, Boone *et al* 1997). However, in all these techniques, electrodes are the inevitable means to obtain data from the conductive body. They are used either to introduce energy by current injection or to measure voltages from the body surface, or for both purposes. In applied-current electrical impedance tomography (ACEIT), current injection and voltage measurements are both performed by the surface electrodes (Barber and Brown 1983, 1984, Isaacson 1986, Ider *et al* 1990). In induced-current electrical impedance tomography (ICEIT), currents are introduced by magnetic induction and voltages are measured using the surface electrodes (Purvis *et al* 1993, Gencer *et al* 1994, 1996, Freeston and Tozer 1995). However, there are several limitations related to electrodes and associated cabling (Purvis *et al* 1993, Gencer *et al* 1996). In addition, electrode placement and recording of their precise locations are important problems in practice (Ider *et al* 1992).

Recently, a new imaging modality has been proposed as an alternative to the mentioned techniques to image the electrical conductivity of human tissues via contactless measurements

† E-mail address: `ngencer@ed.eee.metu.edu.tr`

(Gencer and Tek 1998). In this modality, currents are induced in the conductive body by time-varying magnetic fields. The magnetic fields of induced currents are measured via coils placed near the conductive body surface. Note that this measurement methodology has been known for decades. It has been used to measure the salinity of sea water and the impurity content in metals and semiconductors (Tarjan and McFee 1968). In the field of geophysics it is an important tool for geophysical inspection (Kaufman and Keller 1989, Wait 1982). For medical purposes it was used by Tarjan and McFee (1968) to determine the effective resistivity of the human torso and head. However, it has not been used to image the conductivity distribution of living tissues. Note that since the measurements are contactless, data collection will be considerably easier for the proposed system. In addition, the new system has the following relative merits:

(a) It is possible to couple currents into deep-lying tissues, thus avoiding the screening effect of bones, which is an important disadvantage for modalities that use the current injection technique.

(b) This modality can double the number of independent measurements by a simple shift in the sensor positions. Further increase in the number of measurements can be achieved by using a scanning mechanism. Contrary to the magnetic system, increasing the number of independent measurements is a serious problem for a system based on surface potential measurements.

Wait (1982) has derived analytical expressions for the solution of the magnetic fields above a conducting half-space for the purpose of geophysical explorations. These expressions were used to understand the feasibility of the measurement system for imaging purposes in biomedicine (Gencer and Tek 1998). In that study, circular coplanar coils of radius 1 cm located 1 cm above a uniform conductive half-space of conductivity 0.2 S m^{-1}. The single-turn transmitter coil was excited by sinusoidal current of peak 1 A at 50 kHz. The number of turns of the receiver coil has 10 000 turns and it was placed 5 cm away from the transmitter coil. Note that the received electromotive force should have two components: the primary voltage which is directly coupled from the transmitter coil and the secondary voltage created by the induced currents. The primary and secondary voltages are calculated as 250 mV and 11.4 μV respectively. The maximum induced current density was obtained as 4.9×10^{-4} mA cm^{-2} which is much smaller than the safety limit of 1.6 mA cm^{-2} (Ghahary 1990) for that operation frequency. Note that the secondary voltages are measurable and can be increased by adjusting several parameters, i.e. the number of turns in both coils, the current in the transmitter coil, the operation frequency, distance between coils, etc (a brief discussion on the measurement accuracy is given in section 4). The validity of two important assumptions was also justified by Gencer and Tek (1998): for operation frequencies below 100 kHz the displacement currents are negligible and the propagation effects can be ignored for a typical survey distance in the human body.

Analytical expressions are useful for analysing field patterns for simple geometries. However, they do not provide insight into the measurement sensitivity to local conductivity variations. A numerical method has to be developed to find the magnetic fields of induced currents for objects of arbitrary geometries and conductivity distributions. This will provide a means, for example, to investigate the field patterns associated with single-voxel perturbations at different depths. The numerical model will also form the basis of the imaging system. A possible inverse problem solution, i.e. determination of the conductivity distribution using a set of magnetic field measurements, will definitely depend on a numerical model that provides solutions for an assumed conductivity distribution.

In this study, a numerical model developed using finite element method (FEM) is presented. The accuracy of the solutions is tested for the standard problems in the literature. An analytical expression is also derived to test fields for a homogeneous spherical body. The development of such a numerical model allows us to analyse the fields of single-voxel perturbations at different depths for different coil configurations. The strengths and spatial distribution of fields provide information about the coil configuration of a possible imaging system.

2. Forward problem formulation

A magnetic excitation magnetic detection system uses time varying magnetic fields to induce currents inside conductive body and measures the magnetic fields caused by the induced currents. Thus the electromagnetic problem can be defined as solving the secondary magnetic fields due to a sinusoidally varying current in a transmitter coil nearby a conductive body. The following set of Maxwell's equations govern the behaviour of sinusoidally varying (e^{jwt} time dependence is assumed) electromagnetic fields in a linear, non-magnetic, isotropic, source-free, conductive medium (Plonsey 1961):

$$\nabla \times \boldsymbol{E} = -j\omega\mu\boldsymbol{H} \qquad \nabla \cdot \boldsymbol{E} = 0$$
$$\nabla \times \boldsymbol{H} = (\sigma + j\omega\epsilon)\boldsymbol{E} \qquad \nabla \cdot \boldsymbol{B} = 0$$

(1)

with the continuity equation

$$\nabla \cdot \boldsymbol{J} = 0.$$

(2)

The auxiliary equations that define the characteristics of the medium are given as

$$\boldsymbol{D} = \epsilon\boldsymbol{E}$$
$$\boldsymbol{J} = \sigma\boldsymbol{E}$$
$$\boldsymbol{B} = \mu\boldsymbol{H}.$$

(3)

The symbols $\boldsymbol{E}$, $\boldsymbol{J}$, $\boldsymbol{D}$, $\boldsymbol{H}$ and $\boldsymbol{B}$ are the electric field, current density, electric displacement, magnetic field intensity and magnetic flux density respectively in complex phasor notation. Here the radial frequency is denoted by ω. The material constants, namely conductivity, permittivity and permeability, are represented by σ, ϵ and μ respectively.

Magnetic vector potential $\boldsymbol{A}$ is an auxiliary vector field ($\boldsymbol{B} = \nabla \times \boldsymbol{A}$) which is usually used to calculate the electric field $\boldsymbol{E}$ more conveniently:

$$\boldsymbol{E} = -j\omega\boldsymbol{A} - \nabla\phi.$$

(4)

This shows that the electric field has two sources: change of the magnetic field with time, and charge accumulation. In order to compute the electric field these two potentials, $\boldsymbol{A}$ and ϕ, must be calculated. According to the Helmholtz theorem, a vector function is completely specified if its divergence and curl are known. When the divergence of $\boldsymbol{A}$ is set to zero (i.e. under Coulomb's gauge conditions), we obtain a Helmholtz equation for which the solution is

$$\boldsymbol{A} = \frac{\mu_0}{4\pi} \int \frac{\boldsymbol{J}\,e^{-jkR}}{R}\,dV$$

(5)

where R is the distance between the current source and field points, V denotes the volume of current sources and k is the wave number expressed as

$$k^2 = j\omega\mu\sigma - \omega^2\epsilon\mu.$$

(6)

For quasistatic fields the propagation effects are assumed to be negligible, that is the e^{-jkR} term in the integrand is replaced by unity and the solution for A reduces to the one obtained for the static case

$$A = \frac{\mu_0}{4\pi} \int \frac{J}{R} \, dV. \tag{7}$$

Note that A calculated in this way is the primary magnetic vector potential that exists when the conductive object is not present; in other words the effects of the conductive object are ignored. Assuming that the displacement currents are negligible compared with the conduction currents ϕ can be obtained by the following partial differential equation (Gencer *et al* 1994):

$$\nabla \cdot (\sigma \nabla \phi) = -\nabla \sigma \cdot j\omega A \qquad \text{in } V \tag{8}$$

$$\frac{\partial \phi}{\partial n} = -j\omega A_n \qquad \text{on } S \tag{9}$$

where n represents the outward normal on S, A_n is the normal component of A on S and V denote the conductive body volume. Note that under the adopted assumptions, the real part of the scalar potential is zero (Gencer 1994) yielding

$$E = -j(\omega A + \nabla \phi). \tag{10}$$

Thus, the induced current density J_i can simply be obtained by

$$J_i = -j\sigma (\omega A + \nabla \phi). \tag{11}$$

These currents are the basis of the secondary magnetic field B_s that reflects the properties of the conductive object. B_s can be calculated by using the Biot–Savart law:

$$B_s = \frac{\mu_0}{4\pi} \int \frac{J_i \times R}{R^3} \, dV \tag{12}$$

where μ_0 is the free space permeability, R is the vector from the source point to the field point and R is the distance between them.

3. Numerical solution of the forward problem

The solution of the forward problem requires the solution of partial differential equations governing the scalar potential function ϕ. For that purpose, finite element method (FEM) is employed (Tek and Gencer 1997). This allows one to take into account the inhomogeneity and anisotropy in the conductivity of tissues. The FEM formulation developed in this study is presented in appendix A. The performance of the numerical model is tested with analytical solutions and with the results reported for standard problems. Thereafter, simulation studies are carried out to analyse the effect of conductivity perturbations to the magnetic field measurements.

3.1. Accuracy of numerical solutions

In this study, the performance of the numerical model is tested for three sample problems. In the first case, the potential distribution in a spherical conductive body is calculated. In the other two cases, potentials are calculated for a homogeneous conductive cube. Solutions are obtained assuming isotropic and anisotropic conditions.

In the first sample problem, a circular coil of radius 5 cm carrying a sinusoidal current of 1 A at 50 kHz is placed in the $z = 0$ plane. The coil encircles the spherical body of radius 1 cm. The origin is selected as the centre of the sphere and the coil centre is placed to $x = 3$ cm.

Table 1. Comparison of analytical and numerical (FEM) results of the scalar potential for the spherical object.

x (cm)	y (cm)	FEM (mV)	Analytical (mV)	% Error
0.00	1.00	0.702	0.703	0.16
−0.20	0.98	0.696	0.698	0.37
−0.38	0.92	0.665	0.667	0.28
−0.55	0.83	0.606	0.609	0.53
−0.71	0.71	0.521	0.523	0.50
−0.83	0.55	0.409	0.413	0.97
−0.92	0.38	0.286	0.288	0.76
−0.98	0.20	0.148	0.150	1.07
−1.00	0.00	0.000	0.000	0
−0.98	−0.20	−0.150	−0.151	1.12
−0.92	−0.38	−0.287	−0.289	0.76
−0.83	−0.55	−0.410	−0.414	0.97
−0.71	−0.71	−0.522	−0.525	0.50
−0.55	−0.83	−0.607	−0.611	0.52
−0.38	−0.92	−0.666	−0.668	0.30
−0.20	−0.98	−0.696	−0.699	0.36
0.00	−1.00	−0.702	−0.703	0.16
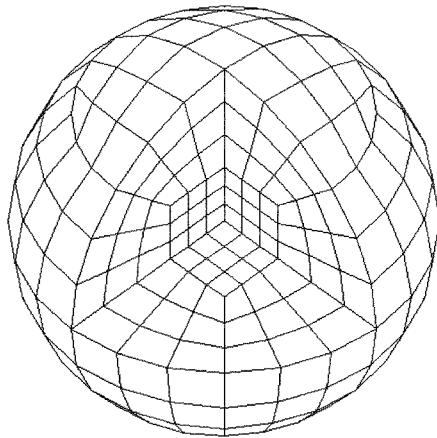
Figure 1. The spherical mesh of 1201 nodes and 256 elements.

The conductivity of the sphere is $0.2\ \mathrm{S\ m^{-1}}$. The scalar potentials are calculated at the selected points on the sphere surface at the $z = 0$ plane. The coordinates and numerical results are given in table 1. In order to test the accuracy of solutions, an analytical expression is derived and given in appendix B. Table 1 shows that the error on the numerical solutions is less than 2% when a spherical mesh composed of 1201 nodes and 256 elements (figure 1) is used for calculations.

In the other tests, FEM solutions are obtained for a homogeneous conductive cubic slab excited by a uniform magnetic field of 1 T at 1 rad s^{-1}. These conditions simulate the transient fields in magnetic resonance imaging (Wang and Eisenberg 1994). The size of the slab is 0.2 m, 0.15 m and 0.1 m in the x, y and z directions respectively. When the cube has isotropic conductivity of $1\ \mathrm{S\ m^{-1}}$ the analytical and 3D FEM solutions of the maximum current density are reported as $6.02 \times 10^{-2}\ \mathrm{A\ m^{-2}}$ and $6.00 \times 10^{-2}\ \mathrm{A\ m^{-2}}$. In this study, a cubic FEM mesh with

4961 nodes is generated and the maximum current density is calculated as 6.03×10^{-2} A m^{-2} for the same problem. When the cube is anisotropic ($\sigma_x = \sigma_z = 1$ S m^{-1}, $\sigma_y = 0.1$ S m^{-1}) the maximum current density is calculated as 2.31×10^{-2} A m^{-2} whereas it is reported as 2.3×10^{-2} A m^{-2} (Wang and Eisenberg 1994).

3.2. Comparison of conductive half-space and cubic body

In an earlier work (Gencer and Tek 1998), the secondary voltage and the maximum value of the induced currents were calculated for a representative coil configuration over a conductive half-space using analytical formulations. In this study, a simulation is performed using the numerical model to verify the order of magnitudes of the previously calculated values (figure 2). The coil configuration is chosen similar to the one used in the previous work. In that study, the radius of the transmitter and receiver coils was 1 cm and the number of turns of the receiver coil was 10 000. The single-turn transmitter coil was excited by a sinusoidal current of 1 A at 50 kHz. The coils were in a coplanar configuration, that is they were located 1 cm above the conductive object in the x–y plane and the distance between them was selected to be 5 cm. In the simulation study, since the length of the body is 9 cm, the coils are placed 2.5 cm apart in order to minimize the effects of edges. The secondary voltage on the receiver coil is calculated to be $1.30\ \mu$V while the maximum induced current in the conductive body is 1.43×10^{-4} mA cm^{-2}. Note that, for the conducting half-space problem the secondary voltage and the maximum current density were calculated as $11.4\ \mu$V and 4.9×10^{-4} mA cm^{-2} respectively. Thus the order of magnitudes for induced currents and voltages are consistent for the two cases. The differences in these values should originate from the differences in the sizes of the conducting spaces, the effects of charge accumulation at the edges of the cubic body, and the difference in the distance between the transmitter and receiver coils.
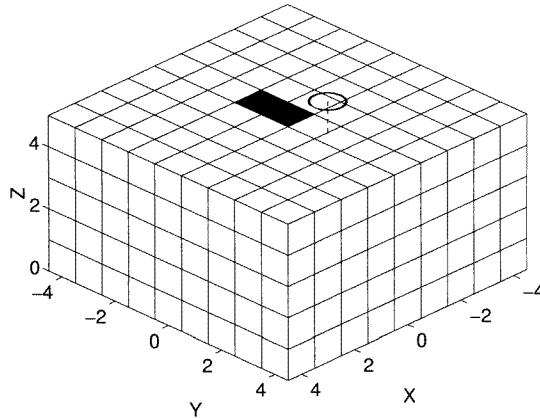
Figure 2. The configuration of the sample problem.

3.3. Field patterns associated with single-voxel perturbations

The aim of the imaging system is to determine the conductivity variations from the magnetic field measurements. Consequently it is necessary to understand the effect of conductivity perturbations on the magnetic field measurements. For that purpose, a representative problem is defined and this effect is analysed.

Figure 2 shows a cubic object of conductivity 0.2 S m^{-1}. The body length is 9 cm in the x direction, 9 cm in the y direction and 5 cm in the z direction. For the FEM solutions, the body is divided into 405 voxels of size $1 \times 1 \times 1$ cm. The cubic body is excited by a transmitter coil of radius 0.5 cm located at $(0, 0.5, 6)$. The coil current is 1 A and operation frequency is 10 kHz.

In order to obtain a reference, the potential distribution (ϕ_0) and the secondary magnetic field pattern (B_{s0}) are obtained when the body is uniform in conductivity. Thereafter, a single voxel at centre of each x–y layer is perturbed to 0.22 S m^{-1} and the associated fields (ϕ and B_s) are solved. This process is repeated for the upper four layers. The changes in the potential ($\phi - \phi_0$) distribution and the magnetic field patterns ($B_s - B_{s0}$) are presented in figure 3. Note that the potential patterns are always displayed on the top surface ($z = 5$ cm) whereas the magnetic fields are calculated 0.5 cm above it ($z = 5.5$ cm). Thus voxel perturbation on the upper surface produces a slightly larger spread in the magnetic field patterns compared with the potential pattern (figures 3(a) and (e)). The field patterns would have similar spread if the magnetic fields were calculated exactly on the upper surface of the body. The other pairs obtained for deeper voxel locations show that there is less spread in the magnetic field patterns. However, in general it is observed that a conductivity perturbation causes changes in the potential and magnetic fields similar to the field patterns of a current dipole (figure 3). The direction of the dipole is parallel to the direction of the magnetic vector potential caused by the transmitter coil at that point. When the perturbation is at deeper locations, peaks of the patterns separate and the magnitudes decrease. It can be inferred that the field magnitude reduces approximately ten-fold for a depth increase of 1 cm. This shows that the SNR of the measurement system will be critical to sense deep voxel perturbations.

In order to analyse the effects of coils located in planes vertical to the x–y plane, field patterns are observed for two coil orientations. For that purpose, the transmitter coil is placed first in the y–z plane and then in the x–z plane. The centre of the transmitter coil is not altered. Figure 4 shows the change in the magnetic field and potential patterns for the two coil configurations when two voxels are perturbed on the x–y plane. It is observed that rotating the transmitter coil from the x–y plane to the y–z plane does not affect the field magnitudes. However, the direction of the observed dipole pattern is aligned to the direction of the magnetic vector potential, since the charge accumulation occurs at the conductivity interfaces where the magnetic vector potential intersects the boundaries of the conductivity perturbation (see equation (8)). The boundaries of the conductivity perturbations are followed by the peaks of the field pattern. The distance between the peaks of the field patterns is a measure of the perturbation length, but this also depends on the perturbation depth.

3.4. Speed and memory requirements

In this study, the numerical model is implemented in C++ and the results are obtained using an Intel Pentium 166 MHz PC. In the sphere problem, a 1201-noded mesh is used to evaluate the scalar potential and the computation time is 8 s with a memory consumption of less than 2 MB. Comparison with the analytical results showed that FEM solutions introduce an error of less than 2%. A cubic object test also approved the speed and accuracy in the FEM solutions: a 4961-noded mesh is solved in 37 s and the error on the peak value is less than 1%. It is found that the forward problem can be solved with PCs in reasonable time periods. Solution time will become more important if an imaging algorithm is based on the iterative use of the forward problem.
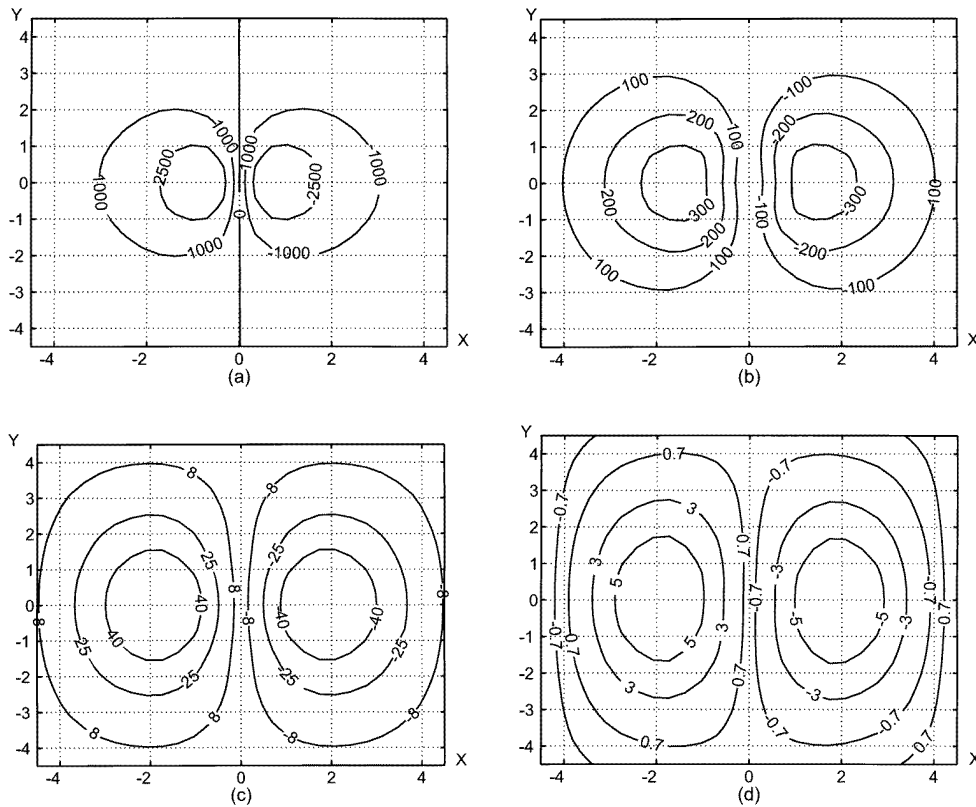
Figure 3. Field patterns for single-voxel perturbations. Change in the z component of the secondary magnetic field patterns ($\times 10^{-22}$ Wb cm^{-2}) for a single-voxel perturbation at (*a*) $z = 4.5$ cm, (*b*) $z = 3.5$ cm, (*c*) $z = 2.5$ cm, (*d*) $z = 1.5$ cm. Change in the scalar potential distribution ($\times 10^{-9}$ V) for a single-voxel perturbation at (*e*) $z = 4.5$ cm, (*f*) $z = 3.5$ cm, (*g*) $z = 2.5$ cm, (*h*) $z = 1.5$ cm. The plots of the potential distributions are calculated on the top surface of the object ($z = 5$ cm) whereas the magnetic field distributions are calculated at the $z = 5.5$ cm plane.

4. Conclusion and discussions

In this study, the numerical solution of the forward problem of a new medical imaging modality is explored. This modality provides tissue conductivity distribution via contactless measurements. For that purpose, currents are induced in the body using time-varying magnetic fields and the magnetic fields of the induced currents are measured. It was found that measurable signal levels can be achieved when induced currents in the tissues are within the safe level (Gencer and Tek 1998). In that study the conductive object was assumed to be an infinite half-space. However, numerical model enabled us to question signal levels and the field patterns for more realistic geometries.

4.1. Field patterns

Field patterns carry important information about the performance of the proposed imaging system. It is obvious that conductivity changes are followed by the secondary magnetic fields,
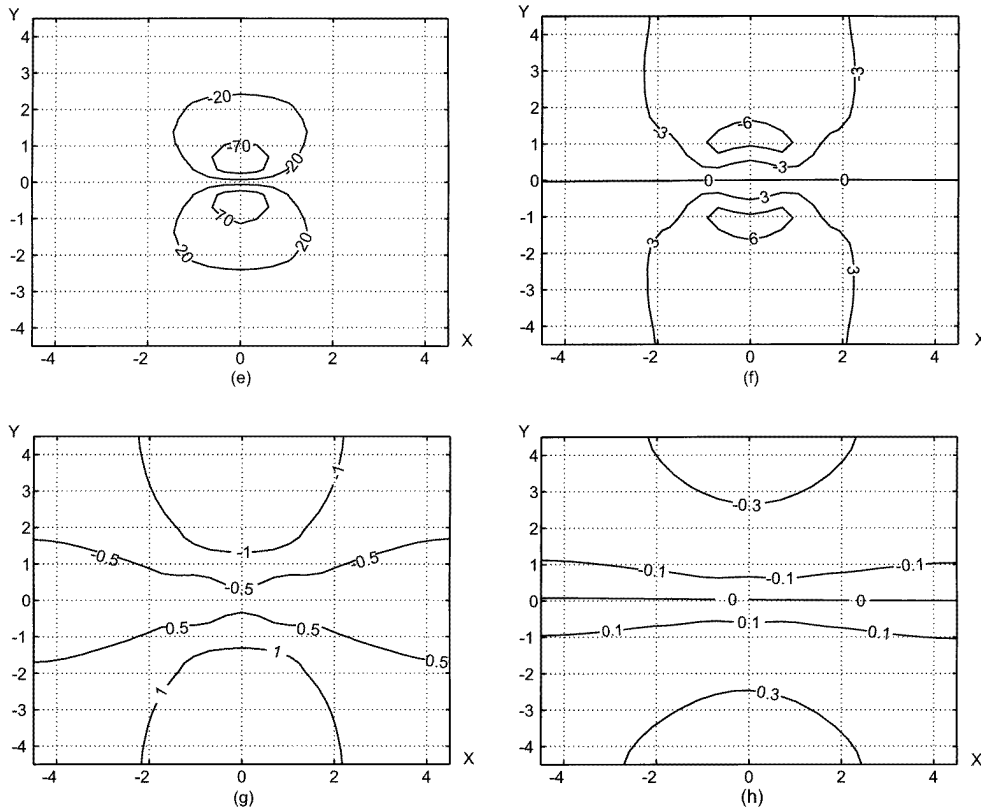
Figure 3. (Continued)

which are the candidate measurements of the proposed system. The effect of a single-voxel conductivity perturbation cause changes in the potential and magnetic field patterns that are similar to the field patterns of a current dipole. With an increase in the perturbation depth, the peaks of the field patterns separate and magnitudes decrease. Increasing the depth of the perturbed voxel decreases the magnitude of the field pattern to approximately one-tenth of its original value. This means that SNR of the measurement system will determine the maximum depth where perturbations can be imaged. Placing the transmitter coil to x–y, y–z or x–z planes does not cause significant difference in the field magnitudes. However, by rotating the coil plane around the coil centre it is possible to scan the perturbation boundaries and obtain independent data. Data collection for imaging algorithms can be achieved by either rotating or moving the transmitter coil. The spatial frequency of the magnetic field pattern is critical since measurements must sample this pattern properly. It is found that for the mentioned configuration, higher spatial frequencies are observed when the perturbation is closer to the coils.

4.2. Required accuracy in the magnetic field measurements

Note that the receiver coil measures the sum of the primary and secondary voltages, and the ratio between these components is approximately 20 000:1. In order to reveal the data
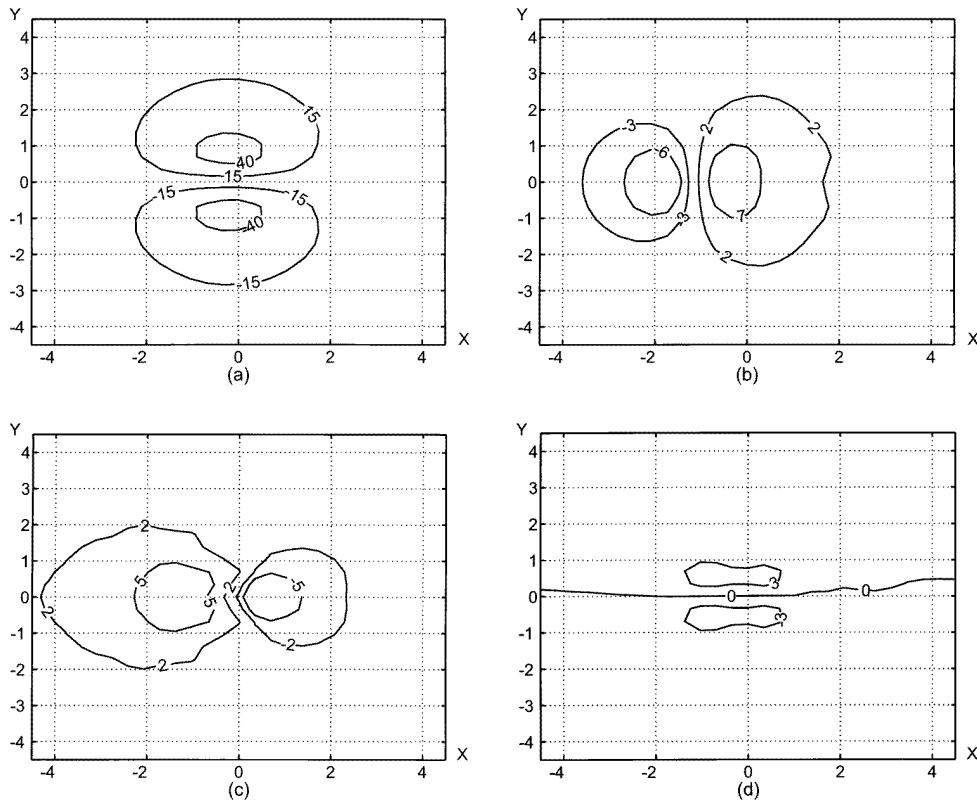
Figure 4. Field patterns for two-voxel perturbations. Perturbed voxels and the transmitter coil are shown in figure 2. The centre of the perturbed voxels are located at $(0, 0, 4.5)$ and $(-1, 0, 4.5)$ in cm. (*a*), (*b*) Changes in the z component of the secondary magnetic fields ($\times 10^{-20}$ Wb cm^{-2}); (*c*), (*d*) changes in the potentials ($\times 10^{-8}$ V) calculated at the same location as in figure 2. Note that (*a*) and (*c*) are obtained when the transmitter coil lies in the y–z plane and (*b*) and (*d*) are obtained when it lies in the x–z plane.

(i.e. the secondary voltages) the primary voltages must be removed from the measurements with sufficient accuracy. Measurement of the secondary voltages to an accuracy of 1% requires a cancellation of the primary voltage by one part in 2 million.

One way of eliminating the primary voltages is to place a receiver coil at each side of the transmitter (Tarjan and McFee 1968). These coils are connected in series phase opposition to provide a null signal when there is no conductive body near the coil system. When the coils are placed closer to a body, the distant coil measures only the direct coupling but the nearby coil is sensitive to both primary and secondary fields. If the primary voltages exactly cancel each other, the resultant signal reflects the secondary fields of the induced currents in the conductive body. In practice, it is not possible to obtain exact cancellation because of inadequate precision in the coil parameters. The residual signal is minimized by a corrective RLC network. In addition, an electrostatic shielding system is used to minimize the imbalance caused by the differences in capacitance between the body and the receiver coils. Note that by using these techniques and manual adjustments, Tarjan and McFee (1968) achieved an overall cancellation of about one part in 10 million satisfying the required accuracy in measurements.

A possible imaging system should employ an array of coils to detect fields at a number of locations. Thus, if a cancellation mechanisms is to be used the system should be designed to perform such calibrations automatically.

The performance of the new imaging modality depends on different parameters associated with the measurement system (like the operating frequency, the coil configuration, current in the transmitter coil, and distance to the conductive object). Thus further studies should be carried out on the optimization of such parameters. In addition, studies on the inverse problem, i.e. calculation of the conductivity distribution using the magnetic measurements, is inevitable. At this point it can be stated that if this new imaging modality can be made to work, it will be useful tool for following spatio-temporal behaviour of electrical conductivity of biological tissues via contactless measurements.

Acknowledgment

Appendix A. FEM formulation

The FEM formulation for the solution of the scalar potential function for magnetic induction problems was given in Tek and Gencer (1997). In that formulation, the conductive body was assumed to be isotropic. In the present study, the formulation is extended to allow anisotropic conductivity distributions.

Anisotropic conductivity of an object is represented with a conductivity tensor:

$$\sigma = \begin{bmatrix} \sigma_{11} & \sigma_{12} & \sigma_{13} \\ \sigma_{21} & \sigma_{22} & \sigma_{23} \\ \sigma_{31} & \sigma_{32} & \sigma_{33} \end{bmatrix}. \tag{A1}$$

Note that this tensor will be constant for each element, and inhomogeneity of the medium is represented with the variation of tensors in the elements. In our study, 20-noded isoparametric, quadratic, hexahedral element types are preferred (figure 5).

$$x(\eta, \xi, \gamma)$$
$$y(\eta, \xi, \gamma)$$
$$z(\eta, \xi, \gamma)$$
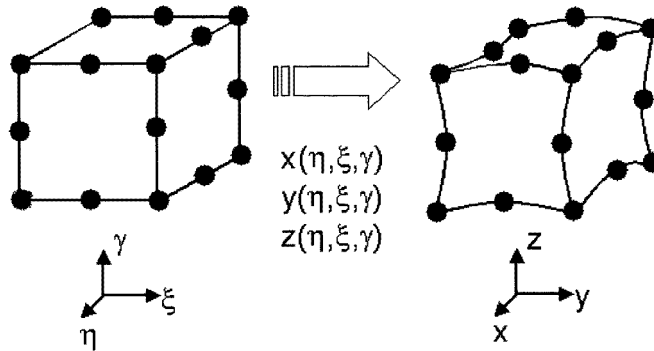
Figure 5. Mapping from local coordinates (η, ξ, γ) to global coordinates (x, y, z) for 20-noded hexahedral elements.

The starting point of the FEM formulation is the partial differential equation governing the imaginary part of the scalar potential function. Applying Galerkin's weighted residuals

method to (8)

$$\int N_i \nabla \cdot (\sigma_e \nabla \phi) \, dV_e = - \int N_i \nabla \sigma_e \cdot \omega \mathbf{A} \, dV_e \tag{A2}$$

is to be satisfied for each quadratic shape function, N_i, $i = 1, \ldots, 20$. Here and in the other equations the subscript e is used to show that integrations are taken in the element volume and on the element surface. Assuming constant conductivity in each element ($\nabla \sigma_e = 0$) and using divergence theorem

$$\int N_i \sigma_e \nabla \Phi \cdot d\mathbf{S}_e = \int \nabla N_i \cdot (\sigma_e \nabla \Phi) \, dV_e. \tag{A3}$$

The $\sigma_e \nabla \Phi$ term on the right-hand side of (A3) should be evaluated before the dot product as

$$\sigma_e \nabla \Phi = \sum_{j=1}^{20} \left[\left(\sigma_{11} \frac{\partial N_j}{\partial x} + \sigma_{12} \frac{\partial N_j}{\partial y} + \sigma_{13} \frac{\partial N_j}{\partial z} \right) \mathbf{a}_x + \left(\sigma_{21} \frac{\partial N_j}{\partial x} + \sigma_{22} \frac{\partial N_j}{\partial y} + \sigma_{23} \frac{\partial N_j}{\partial z} \right) \mathbf{a}_y \right.$$

$$\left. + \left(\sigma_{31} \frac{\partial N_j}{\partial x} + \sigma_{32} \frac{\partial N_j}{\partial y} + \sigma_{33} \frac{\partial N_j}{\partial z} \right) \mathbf{a}_z \right] \Phi_j$$

$$= \sum_{j=1}^{20} (K_{xj} \mathbf{a}_x + K_{yj} \mathbf{a}_y + K_{zj} \mathbf{a}_z) \Phi_j = \sum_{j=1}^{20} \mathbf{K}_j \Phi_j. \tag{A4}$$

Handling the left-hand side of (A3) requires care since (9) is not valid for anisotropic conditions. Instead, the new form of this boundary condition is represented as follows:

$$(\sigma_e \nabla \Phi) \cdot \mathbf{n} = (\sigma_e \omega \mathbf{A}) \cdot \mathbf{n}. \tag{A5}$$

With this new representation and remembering that $d\mathbf{S}_e = \mathbf{n} \, dS_e$, (A3) becomes

$$\int N_i (\sigma_e \omega \mathbf{A}) \cdot \mathbf{n} \, dS_e = \sum_{j=1}^{20} \int \nabla N_i \cdot \mathbf{K}_j \Phi_j \, dV_e. \tag{A6}$$

The $\sigma_e \omega \mathbf{A}$ term should also be evaluated before its dot product with the surface normal as

$$\sigma_e \omega \mathbf{A} = \omega[(\sigma_{11} A_x + \sigma_{12} A_y + \sigma{13} A_z) \mathbf{a}_x + (\sigma_{21} A_x + \sigma_{22} A_y + \sigma{23} A_z) \mathbf{a}_y$$

$$+ (\sigma_{31} A_x + \sigma_{32} A_y + \sigma{33} A_z) \mathbf{a}_z] \tag{A7}$$

$$= P_x \mathbf{a}_x + P_y \mathbf{a}_y + P_z \mathbf{a}_z = \mathbf{P}. \tag{A8}$$

Placing the new representation to (A6)

$$\sum_{j=1}^{20} \int \nabla N_i \cdot \mathbf{K}_j \Phi_j \, dV_e = - \int N_i \mathbf{P} \cdot \mathbf{n} \, dS_e. \tag{A9}$$

If the same process is repeated for $i = 1, \ldots, 20$ the element matrix equation is formed:

$$\mathbf{M}\Phi^e = b^e \tag{A10}$$

where entries of the matrix $\mathbf{M}$ and vector b^e are

$$\mathbf{M}(i, j) = \int \nabla N_i \cdot \mathbf{K}_j \, dV_e$$

$$b^e(i) = - \int N_i \mathbf{P} \cdot \mathbf{n} \, dS_e. \tag{A11}$$

Here the surface and volume integrations are evaluated using the local coordinates (figure 5) by applying 9- and 27-point Gauss integration procedures respectively. All element matrix

equations can be assembled to obtain a linear set of equations relating the unknown node potentials to the excitation parameters. In matrix form, this can be written as follows

$$\mathbf{A}\boldsymbol{\Phi} = \boldsymbol{b}. \tag{A12}$$

If N denotes the total number of nodes, then $\mathbf{A}$ is an $N \times N$ matrix that includes geometry and estimated conductivity information, $\boldsymbol{\Phi}$ is ann $N \times 1$ vector of node potentials, and $\boldsymbol{b}$ is an $N \times 1$ vector of excitation. Since $\mathbf{A}$ is large in dimension but sparse, solution of $\boldsymbol{\Phi}$ is obtained by conjugate gradient method.

Appendix B. Sphere problem

A series expansion solution of scalar potential on a spherical homogeneous conductive object can be written as (Plonsey and Collin 1961, p 141)

$$\phi(r, \theta, \zeta) = \sum_{l=0}^{\infty} \sum_{k=0}^{l} (A_k \cos k\zeta + B_k \sin k\zeta) C_l r^l P_l^k(\cos\theta) \tag{B1}$$

where r, θ and ζ represent the spherical coordinate system, $P_l^k()$ denotes the Legendre function and ϕ is the scalar electric potential in this section. Rearranging the unknown series coefficients ($a_{kl} = A_k.C_l$ and $b_{kl} = B_k.C_l$), the expression can be rewritten as

$$\phi(r, \theta, \zeta) = \sum_{l=0}^{\infty} \sum_{k=0}^{l} (a_{kl} \cos k\zeta + b_{kl} \sin k\zeta) r^l P_l^k(\cos\theta). \tag{B2}$$

Derivation of the series coefficients can be performed by applying (9) to the expression and making use of the orthogonality properties of sine and Legendre functions. Details of the derivation can be found in Tek and Gencer (1997). The coefficients a_{kl} and b_{kl} of the series are

$$a_{kl} = -\omega \frac{(2l+1)(l-k)!}{2\pi l r^{l-1}(l+k)!} \int_0^{\pi} \int_0^{2\pi} A_n P_l^k(\cos\theta) \cos k\zeta \, \mathrm{d}\zeta \, \sin\theta \, \mathrm{d}\theta \tag{B3}$$

$$b_{kl} = -\omega \frac{(2l+1)(l-k)!}{2\pi l r^{l-1}(l+k)!} \int_0^{\pi} \int_0^{2\pi} A_n P_l^k(\cos\theta) \sin k\zeta \, \mathrm{d}\zeta \, \sin\theta \, \mathrm{d}\theta. \tag{B4}$$

In this expression, calculation of series coefficients involves surface integrals which can not be evaluated analytically. Integration step size in the calculation of series coefficients is dependent on the magnetic vector potential variation, A_n. For a transmitter coil of radius 5 cm, accurate solutions on the unit sphere can be obtained where series coefficients are integrated with $\pi/80$ steps. This means that calculation of every coefficient requires 12 800 function evaluations. At this point, the infinite number of terms which are shown in equation (B2) become more critical. It is sufficient to use 20 terms ($l = 20$) to evaluate the scalar potential term correctly for this configuration. However, when the transmitter coil radius is decreased to 0.4 cm, these integrations do not converge with $\pi/250$ step size. Note that reducing the step size brings a computational time of 28 h for 20 coefficients on a Sun Sparc 20 computer. Consequently, computational cost disables the use of this expression with small coils.

References

Barber D C and Brown B H 1983 Imaging spatial distribution of resistivity using applied potential tomography *Electron. Lett.* **19** 933–5
——1984 Applied potential tomography *J. Phys. E: Sci. Instrum.* **17** 723–33
Boone K, Barber D and Brown B 1997 Imaging resistivity with electricity: report of the European Concerted Action on Impedance Tomography *J. Med. Eng. Technol.* **21** 201–32

Freeston I L and Tozer R C 1995 Impedance imaging using induced currents *Physiol. Meas.* **16** (suppl 3A) A257–A266

Gencer N G, Ider Y Z and Williamson S J 1996 Electrical impedance tomography: induced current imaging achieved with a multiple coil system *IEEE Trans. Biomed. Eng.* 43 139–49

Gencer N G, Kuzuoglu M and Ider Y Z 1994 Electrical impedance tomography using induced currents *IEEE Trans. Med. Imaging* **13** 338–50

Gencer N G and Tek M N 1999 Imaging tissue conductivity via contactless measurements: a feasibility study *Turkish J. Elect. Eng. ELEKTRIK* accepted for publication

Ghahary A 1990 *Electrical Impedance Tomography* ed J G Webster (Bristol: IOP Publishing) p 58

Ider Y Z, Gencer N G, Atalar E and Tosun H 1990 Electrical impedance tomography of translationally uniform cylindrical objects with general cross sectional boundaries *IEEE Trans. Med. Imaging* **37** 624–31

Ider Y Z, Kuzuoglu M, Nakiboglu B and Gencer N G 1992 Determination of the boundary of an object inserted into a water-filled cylinder *Clin. Phys. Physiol. Meas.* **13** (suppl A) 155

Isaacson D 1986 Distinguishability of conductivities by electric current tomograph *IEEE Trans. Med. Imaging* **5** 91–5

Kaufman A A and Keller G V 1989 *Induction Logging* (New York: Elsevier)

Morucci J P and Rigaud B 1996 Bioelectrical impedance techniques in medicine *Crit. Rev. Biomed. Eng.* **24** 655–77

Plonsey R and Collin R 1961 *Principles and Applications of Electromagnetic Fields* (New York: McGraw-Hill) p 311

Purvis W R, Tozer R C, Anderson D K and Freeston I L 1993 Induced current impedance imaging *IEE Proc.* **140A** 135–41

Tarjan P P and McFee R 1968 Electrodeless measurements of the effective resitivity of the human torso and head by magnetic induction *IEEE Trans. Biomed. Eng.* **15** 266–78

Tek M N and Gencer N G 1997 A new 3D FEM formulation for the solution of potential fields in magnetic induction problems *Proc. Ann. Int. Conf. of IEEE Eng. Med. Biol. Soc. (Chicago)* p 2470

Wait J R 1982 *Geo-Electromagnetism* (New York: Academic) p 113

Wang W and Eisenberg S R 1994 A three dimensional finite element method for computing magnetically induced currents in tissues *IEEE Trans. Magnetics* **30** 5015–23